Frontiers of Information Technology & Electronic Engineering
www.jzus.zju.edu.cn; engineering.cae.cn; www.springerlink.com
ISSN 2095-9184 (print); ISSN 2095-9230 (online)
E-mail: jzus@zju.edu.cn

Vibration harmonic suppression technology for electromagnetic vibrators based on an improved sensorless feedback control method*#

Wei LI[1,2], Junning CUI†‡[1,2], Xingyuan BIAN[1,2], Limin ZOU[1,2]

[1]*Center of Ultra-precision Optoelectronic Instrument Engineering, Harbin Institute of Technology, Harbin 150080, China*

[2]*Key Lab of Ultra-precision Intelligent Instrumentation (Harbin Institute of Technology), Ministry of Industry and Information Technology, Harbin 150080, China*

†E-mail: cuijunning@hit.edu.cn

Received Jan. 15, 2023; Revision accepted Sept. 6, 2023; Crosschecked Feb. 2, 2024

Abstract: To realize low harmonic distortion of the vibration waveform output from electromagnetic vibrators, we propose a vibration harmonic suppression technology based on an improved sensorless feedback control method. Without changing the original driving circuit, the alternating current (AC) equivalent resistance of the driving coil is used to obtain high-precision vibration velocity information, and then a simple and reliable velocity feedback control system is established. Through the study of the effect of different values of key parameters on the system, we have achieved an effective expansion of the velocity characteristic frequency band of low-frequency vibration, resulting in an enhanced harmonic suppression capability of velocity feedback control. We present extensive experiments to prove the effectiveness of the proposed method and make comparisons with conventional control methods. In the frequency range of 0.01–1.00 Hz, without using any sensors, the method proposed in this study can reduce the harmonic distortion of the vibration waveform by about 40% compared to open-loop control and by about 20% compared to a conventional sensorless feedback control method.

Key words: Vibration calibration; Electromagnetic vibrators; Harmonic suppression; Sensorless control method; Velocity feedback control

https://doi.org/10.1631/FITEE.2300031 **CLC number:** TP271

1 Introduction

Demand for low-frequency vibration calibration accuracy has grown in various fields such as aerospace engineering, precision machining and manufacturing, structural dynamic analysis, earthquake forecasting, tsunami detection and early warning, and the Internet of Things (Crawford and Webb, 2000; Okwudire and Lee, 2013; Addari et al., 2017; Shimoda et al., 2021; Li L et al., 2023a, 2023b). Vibration calibration by electromagnetic vibrators is the most widely used method at present (Scott and Dickinson, 2014; Liu et al., 2021). However, the total harmonic distortion (THD) of the vibration waveform causes uncorrectable errors in the calibration, which should be suppressed as much as possible (ISO, 1999; Ripper et al., 2009).

However, the acceleration amplitude output from an electromagnetic vibrator is proportional to the square of the vibration frequency, and thus the electromagnetic driving force of low-frequency vibration weakens. Many incompletely avoidable micro-interferences, such as the uneven distribution of air-gap magnetic induction intensity (Okyay et al., 2015; Cui et al., 2017, 2020),

‡ Corresponding author

* Project supported by the Natural Science Foundation of Heilongjiang Province, China (No. LH2021E060), the National Natural Science Foundation of China (No. 52075133), and the CGN-HIT Advanced Nuclear and New Energy Research Institute, China (No. CGN-HIT202215)

Electronic supplementary materials: The online version of this article (https://doi.org/10.1631/FITEE.2300031) contains supplementary materials, which are available to authorized users

ORCID: Wei LI, https://orcid.org/0000-0001-6254-8790; Junning CUI, https://orcid.org/0000-0002-4418-8936

nonlinear stiffness and damping of the suspension device (He et al., 2014), and nonlinear restoring force of the cable (Ohno et al., 2021), all introduce harmonic interference to the low-frequency vibration waveform. Although various advanced control algorithms have been applied to reduce the THD of the vibration waveform (Uchiyama et al., 2009; Rana, 2011; Li C and Chen, 2020; Li C et al., 2022), they are difficult to apply because of the complexity of the mathematical calculations. All the above control methods require suitable vibration sensors. High-precision vibration sensors with a frequency response lower than 0.1 Hz are usually seismometer types, which are too bulky to use in the vibrators, and the use of sensors will reduce system reliability and increase the cost of hardware and maintenance (Wang et al., 2020; Xiao DX et al., 2022; Xiao LF et al., 2022). Hence, a sensorless feedback control method is needed to reduce the THD of the low-frequency vibration waveform.

Sensorless control (also known as self-sensing control) can detect the state of controlled plant without sensors and has the advantages of low complexity, low cost, and high reliability. The high-frequency signal injection method (Shuang et al., 2022), Kalman filter (Yildiz et al., 2020), Luenberger observer (Garrido and Luna, 2021), sliding mode observer (Repecho et al., 2022), and other sensorless control methods have been studied widely. These algorithms have many adjustable parameters, leading to a complex design process, and require a controller with high computational power. For example, in the field of sensorless control of electromagnetic vibrators, Li W et al. (2023) adopted the Kalman filter and used the measured displacement to estimate the vibration velocity of electromagnetic vibrators to establish feedback control. The velocity estimation accuracy of this method depends on the accuracy of parameter adjustment, but the parameter adjustment process is complicated. The low-frequency vibration of an electromagnetic vibrator has a frequency band with large velocity values, which prompted researchers to realize sensorless velocity estimation with induced electric potential. Zhang et al. (2017) and Chi and Shang (2018) constructed a real-time extraction device for induced electric potential by connecting a resistor in series with the electromagnetic vibrator driving circuit to achieve sensorless velocity feedback control. However, such methods ignore the variation of coil resistance with vibration frequency, which leads to low velocity estimation accuracy and changes in the original system structure. As a result, the interference suppression capability of velocity feedback control may decrease.

In light of the above issues, in this study we propose a vibration waveform harmonic suppression technology for electromagnetic vibrators based on an improved sensorless feedback control method. Through the driving current and voltage of the electromagnetic vibrator, we have achieved high precision extraction of the induced electric potential by using the coil alternating current (AC) resistance to establish a sensorless velocity feedback control. This means that there is no need to change the original system structure. We present a theoretical analysis of the rationality of our proposed method. Our group has conducted extensive comparative experiments to verify the superiority of the proposed method. The technical advancements are as follows: (1) The velocity estimation accuracy is improved by adopting the AC resistance of the driving coil. (2) A method for optimizing key parameters is proposed to increase the harmonic suppression capability of velocity feedback control. (3) The harmonic suppression capability of the sensorless velocity feedback control method is improved. The main scientific contribution is the development of an improved sensorless velocity feedback control method, which can effectively reduce the THD of the vibration waveform, improve low-frequency vibration calibration accuracy, reduce the number of sensors, and increase system reliability.

2 Principle

2.1 Basic principle of electromagnetic vibrators

The operating principle of low-frequency dual magnetic circuit horizontal electromagnetic vibrators is shown in Fig. S1 in the supplementary materials. Permanent magnets (PMs) at each end generate a stable magnetic field with an average magnetic induction intensity of B in the air gap through the yokes. A driving coil is placed along the direction perpendicular to the magnetic induction lines, and a driving current i is applied. As a result of the influence of Ampere force on the coil, the moving parts rigidly connect to the

coil and vibrate along an air flotation guide. The vibration displacement is x. The equivalent damping and stiffness of the suspension device are c and k, respectively (He et al., 2014). The stiffness provides a return force $F_r=kx$ for the moving parts to return to the zero position, and the damping produces a damping force $F_c=c\dot{x}$ in the opposite direction of motion. The values of c and k are determined by the form and material of the suspension device. The coil cutting magnetic induction lines in the magnetic field generate an induced electric potential $e=Bl\dot{x}$. Thus, the model of electromagnetic vibrators can be written as (Lang, 1997; Lang and Snyder, 2001)

$$\begin{cases} m\ddot{x} + c\dot{x} + kx = iBl, \\ Ri + L\dot{i} + Bl\dot{x} = u_a, \end{cases} \tag{1}$$

where m is the total mass of moving parts, l is the coil length, R is the coil resistance, L is the coil inductance, and u_a is the driving voltage at each end of the coil. The corresponding transfer function $G_{xu_a}(s)$ is shown in Eq. (2), where $X(s)$ is the form of x after the Laplace transform, $U_a(s)$ is the form of u_a after the Laplace transform, and s is the complex frequency variable. A block diagram of the open-loop system is shown in Fig. 1. The driving voltage u_a subtracts the induced electric potential e to produce the driving current i in the coil, and because of the drive of the electromagnetic driving force iBl on the coil, the moving parts vibrate with displacement x.

$$G_{xu_a}(s) = \frac{X(s)}{U_a(s)} = \frac{Bl}{mLs^3 + (mR + Lc)s^2 + (B^2l^2 + Rc + Lk)s + Rk}. \tag{2}$$

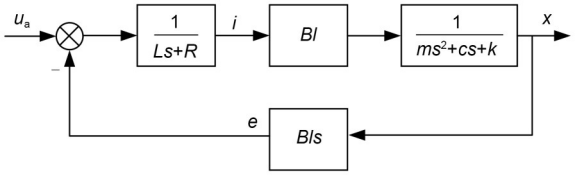

Fig. 1 Block diagram of the open-loop system

Assuming that Eq. (2) has three poles, denoted as p_{o1}, p_{o2}, and p_{o3} (Zhang et al., 2017), and $0<p_{o1}\le p_{o2}\le p_{o3}$, then we have

$$G_{xu_a}(s) = \frac{K_0}{(s - p_{o1})(s - p_{o2})(s - p_{o3})}, \tag{3}$$

$$p_{o1} \approx \frac{Rk}{B^2l^2},\ p_{o2} \approx \frac{B^2l^2}{mR},\ p_{o3} \approx \frac{R}{L}, \tag{4}$$

where $K_0=Bl/(mR)$ is the transmission coefficient of $G_{xu_a}(s)$. According to the actual values of the parameters, $p_{o1}\approx1$ rad/s, $p_{o2}\approx29$ rad/s, $p_{o3}\approx290$ rad/s, and the corresponding corner frequencies are $f_{oi}=p_{oi}/(2\pi)$, where $i=1, 2, 3$. The low-frequency vibration is concentrated mainly in the first two orders of the system, and the Bode diagram (Fig. 2) can be obtained from Eq. (2).

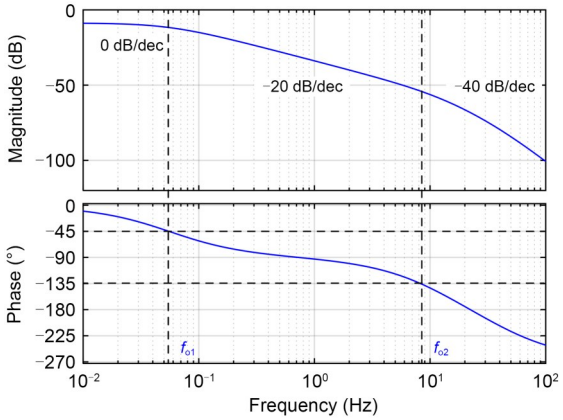

Fig. 2 Bode diagram of Eq. (2)

The real-time and high-precision expression of the feedback information to the system state is the decisive factor enabling the closed-loop feedback control system to achieve good results. Therefore, a feedback signal with a small phase difference from the input and high signal-to-noise ratio must be selected. The slope of the magnitude–frequency curve and the phase difference between the input and output in different frequency bands can be obtained from the Bode diagram to determine a suitable feedback signal. Fig. 2 shows that the corner frequencies $f_{oi}=p_{oi}/(2\pi)$ ($i=1, 2$) divide the low-frequency band of the vibrator's Bode diagram into three bands. In the starting frequency band, the vibration frequency $f<f_{o1}$, the vibration displacement is proportional to the input voltage with a slope of 0 dB/dec, and the phase difference changes from 0° to −45°. As the frequency increases, the slope of the magnitude–frequency curve in each band decays at a rate of −20 dB/dec. The phase difference

increases at a rate of 90°; i.e., in the complex frequency domain, each band increases by s, indicating that the phase difference between the input and the vibration displacement, velocity, and acceleration in each band, separately, is less than 45°. Therefore, when $f<f_{o1}$, namely in the displacement characteristic band, it is suitable for establishing displacement feedback. The phase difference between velocity and input in this band is less than 90°, and the velocity feedback can also play a role in improving the vibration waveform. When $f_{o1}\leq f\leq f_{o2}$, in the velocity characteristic frequency band, it is favorable to establish velocity feedback. When $f_{o2}<f$, in the acceleration characteristic frequency band, it is suitable for setting acceleration feedback control.

2.2 Sensorless velocity extraction method

Conventional sensorless velocity extraction techniques require a sampling resistor R_s connected in series with the driving coil circuit to obtain the driving current. This changes the system characteristics, increases energy consumption, and brings difficulties to parameter adjustment. In addition, there are defects in current shunt measurement complicating the whole process of measurement, such as dissipation, parasitic inductance, and complicated electronics. Moreover, the coil resistance variation at different operating frequencies is ignored in the conventional method, and the velocity information is estimated directly using the driving coil direct current (DC) resistance R_{dc}, which gives misleading results. In the method proposed in this study, the driving voltage u_a and current i are obtained through the power amplifier output monitoring ports without changing the original system structure, which is simpler and more effective. Considering the change of coil resistance under different frequencies, the AC coil resistance R_{ac} comes into play to improve the velocity information extraction accuracy. Thus, the established velocity feedback control can obtain a better harmonic suppression effect in the corresponding frequency band.

Assuming that the driving current is obtained by R_s, then the structure of the driving coil is as shown in Fig. 3, where u_i is the voltage value corresponding to i.

From Fig. 3, let $R'=R+R_s$. The voltage balance equation of the coil is

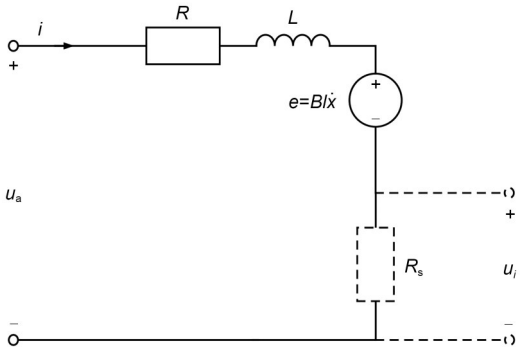

Fig. 3 Schematic of coil structure

$$u_a - R'i = Bl\dot{x} + L\dot{i}. \tag{5}$$

From the force balance equation of the electromagnetic vibrators in Eq. (1), it can be found that

$$X(s)s = \frac{BlI(s)s}{ms^2 + cs + k}, \tag{6}$$

where $I(s)$ is the form of i after the Laplace transform.

At low-frequency vibration, the coil inductance is only at the mH level, and the relationship between the induced electric potential e and the inductance voltage u_L is

$$\frac{e}{u_L} = \frac{BlX(s)s}{LI(s)s} = \frac{B^2l^2}{L(ms^2 + cs + k)} \gg 1. \tag{7}$$

Therefore, $e \gg u_L$, the influence of inductance can be ignored, and the velocity information u_v can be calculated as

$$u_v = Bl\dot{x} = u_a - Ri. \tag{8}$$

A sensorless velocity feedback control system can be established by u_v to suppress the THD of the electromagnetic vibrator output waveform.

3 Establishment of a sensorless feedback control system

According to Fig. 2, the performance of electromagnetic vibrators is similar to that of a low-pass filter. The low-frequency interference signal is the element that passes through the system, causing zero drift of the vibration. A high-pass filter is needed to filter out

the low-frequency interference in the extraction of the velocity signal. The feedback signal processing circuit inevitably has high-frequency noise, and thus a low-pass filter should be adopted. The cut-off frequency of the filter should be away from the vibration frequency to avoid affecting the vibration waveform.

Suppose that the driving current i is obtained by R_s, and that u_v is calculated by R_{dc} of the coil, compared with the reference input signal u through the comparator, and amplified by K_v times. The control deviation E is obtained to realize negative feedback. E is amplified by K_A times by the power amplifier and then inputted to the coil to drive the vibrator. After neglecting the inductance, the system transfer function is

$$G_{xu_a}=\frac{X(s)}{U_a(s)}=\frac{Bl}{mR's^2+(B^2l^2+R'c)s+R'k}. \quad (9)$$

A block diagram of the sensorless velocity feedback control system is illustrated in Fig. 4, where $G_{\dot{x}u_a}=sG_{xu_a}$, d_v is the total harmonic component of $\dot{x}$ caused by the nonlinear factors and other impacts on the vibrator, and d_R is the interference induced by the velocity estimation error when the R_{dc} of the coil is used to calculate u_v.

From Fig. 4, we have

$$\dot{x}=\frac{K_AG_{\dot{x}u_a}}{1+K_vBlK_AG_{\dot{x}u_a}}u+\frac{1}{1+K_vBlK_AG_{\dot{x}u_a}}d_v-\frac{1}{Bl+\dfrac{1}{K_vK_AG_{\dot{x}u_a}}}d_R. \quad (10)$$

The velocity feedback can effectively suppress d_v, reduce the influence of interference, and improve the harmonic distortion of the vibration waveform. The larger the K_v, the stronger the ability to suppress interference. However, as shown in Eq. (10), increasing K_v will further increase the interference of d_R on the vibration velocity $\dot{x}$. As a result, negative velocity feedback control cannot suppress d_R. The R_{ac} should be used to improve the vibration velocity information extraction accuracy and reduce d_R.

Neglecting the disturbances, the system transfer function can be expressed as

$$G_{\dot{x}u}=\frac{\dot{x}}{u}=\frac{K_AG_{\dot{x}u_a}}{1+K_vK_ABlG_{\dot{x}u_a}}=\frac{K_ABls}{mR's^2+(B^2l^2+R'c+K_vK_AB^2l^2)s+R'k}. \quad (11)$$

The velocity characteristic frequency band's bandwidth W_v can be calculated as

$$W_v=\frac{\sqrt{\alpha^2-4\beta}}{2\pi}, \quad (12)$$

where $\alpha=(B^2l^2+R'c+K_vK_AB^2l^2)/mR'$ and $\beta=k/m$. W_v is dependent on R_s and K_v, as shown in Fig. 5. The Bode diagram of $G_{\dot{x}u}$ can more clearly illustrate the change of the velocity characteristic frequency band with the changes of R_s and K_v. The Bode diagrams of different K_v when R_s is a constant value and of different R_s when K_v is a constant value are shown in Figs. S2 and S3 in the supplementary materials, respectively.

W_v is negatively correlated with R_s and positively and more strongly correlated with K_v (Fig. 5 and

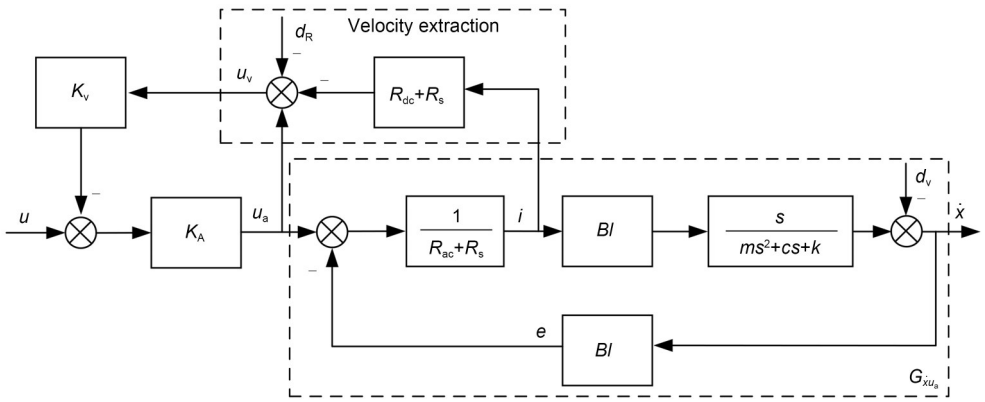

Fig. 4 Block diagram of the system with sensorless velocity feedback control

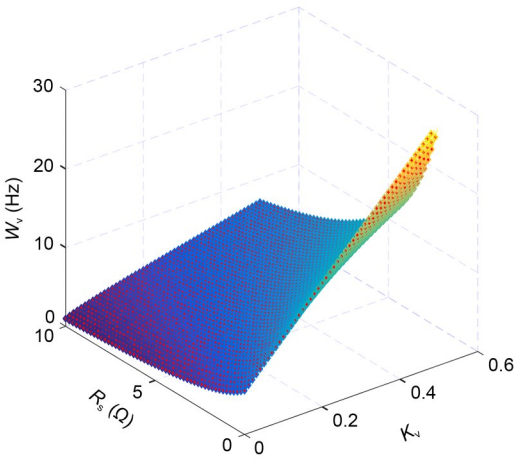

Fig. 5 Relationship among W_v, R_s, and K_v

Figs. S2 and S3). With the widening of the velocity characteristic frequency band, it can be easier to realize the velocity negative feedback in this frequency band and develop the ability to reduce the waveform distortion. Therefore, the value of K_v should be large enough and the value of R_s should be as small as possible, even zero. However, when the feedback coefficient is too large, it may lead to an unstable system. According to Eq. (11), the system root locus of K_v=0⟶∞ can be obtained as shown in Fig. S4 in the supplementary materials, and the root trajectory of the system does not intersect with the imaginary axis. Therefore, the value of K_v will not affect the system stability.

In summary, a larger K_v and a smaller R_s are beneficial to improve the output waveform in the velocity characteristic frequency band of electromagnetic vibrators, and the system can remain stable. As shown in Eq. (10) and Figs. S2 and S3, when R_s and K_v increase, the closed-loop gain of the system decreases; thus, the maximum output voltage amplitude of the signal generator may not satisfy the requirement for the decreased closed-loop gain of the system. Moreover, as K_v increases to a certain level, the interference is suppressed sufficiently, and thus the ability of velocity feedback control to improve the vibration waveform tends to be unchanged. Therefore, a value of K_v should be selected such that its increase no longer significantly increases the velocity feedback control effect, and R_s should be avoided.

4 Experiment

4.1 Experimental setup

The main configuration of the experimental system established according to Fig. 4 is shown in Fig. 6a, and the experimental device is shown in Fig. 6b. The

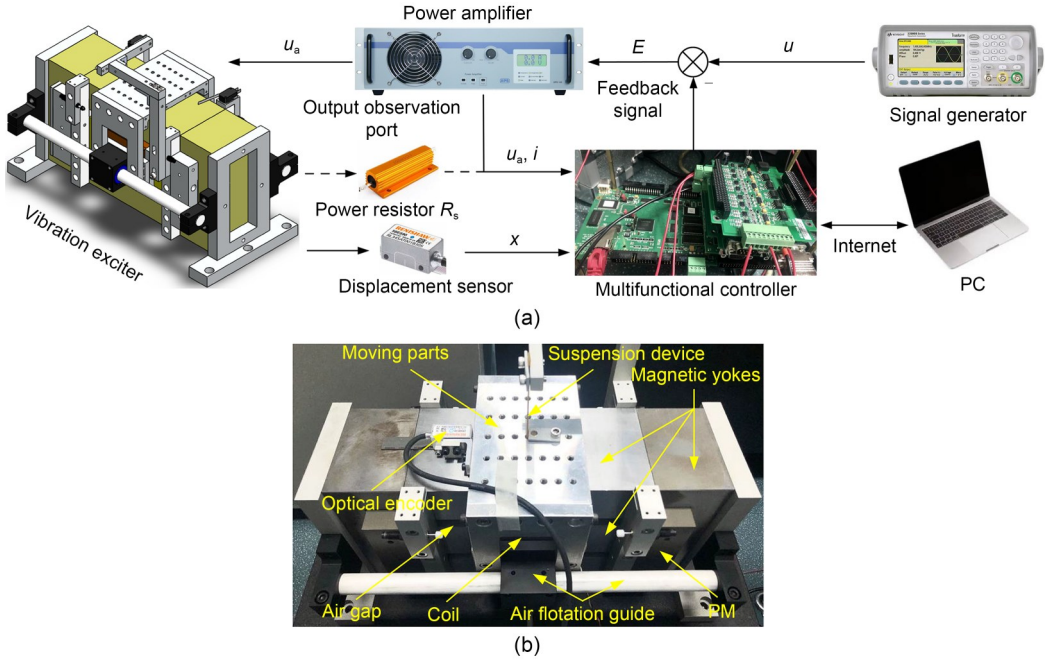

Fig. 6 Low-frequency horizontal electromagnetic vibrator system: (a) main configuration; (b) experimental device (PC: personal computer; PM: permanent magnet)

experimental system consisted of a signal generator with standard sinusoidal voltage output (output range of ±10 V), a power amplifier with an output signal observation function to amplify the control signal, an electromagnetic vibrator (rated travel of 30 mm) to generate standard vibrations, several power resistors with different resistance values as sampling resistors R_s, an optical encoder (resolution of 5 nm) to measure the vibration displacement, and a multifunction controller with an analog-to-digital converter/digital-to-analog converter (ADC/DAC) module (both with 16-bit resolution) and serial encoder, to calculate and output the feedback signal. The experimental ambient temperature was maintained at (26±1) ℃ to prevent the physical characteristics of the coil from being varied by temperature. The signal-to-noise ratio of the accelerometer was insufficient for measuring low-frequency vibrations, and the vibration waveform was evaluated by the displacement signal (Liu et al., 2021). The low-frequency vibration displacement measurement accuracy of an optical encoder is comparable to that of a laser vibrometer (Garg and Schiefer, 2017), and an optical encoder is easier to integrate into the vibrator and has a lower cost. Therefore, the vibration displacement was measured by an optical encoder and transferred to a personal computer (PC) through the controller to complete data processing.

4.2 Experimental vibration level setting

To determine the velocity characteristic frequency band of the electromagnetic vibrator, it is necessary to obtain the magnitude–frequency response characteristics of the system experimentally. The system magnitude–frequency characteristics were tested in the frequency range of 0.003–10.000 Hz. At each experimental frequency, the output voltage amplitude of the signal generator was adjusted to make the electromagnetic vibrator run with full travel, collect the displacement of at least three vibration cycles, and calculate the vibration displacement amplitude. The output voltage amplitude u_p of the signal generator and the vibration displacement amplitude x_p at every test vibration frequency were recorded. Then, the displacement magnitude was $20\lg(x_p/u_p)$ and the corresponding velocity magnitude was $20\lg(2\pi f x_p/u_p)$. Thus, the magnitude–frequency characteristic curves of displacement and velocity were plotted (Fig. 7). From the analysis in Section 2.1, it is clear that in the velocity characteristic frequency band, the slope of the displacement magnitude–frequency characteristic curve was −20 dB/dec, and the slope of the corresponding velocity magnitude–frequency characteristic curve was 0 dB/dec. As a result, the velocity characteristic frequency band of the experimental device was 0.05–1.00 Hz. Therefore, the lower limit of the experimental frequency was 0.01 Hz and the upper limit was 1.00 Hz. The rated travel of the vibration vibrator was 30 mm, and thus the amplitude of the vibration waveform set in the experiment was 15 mm.

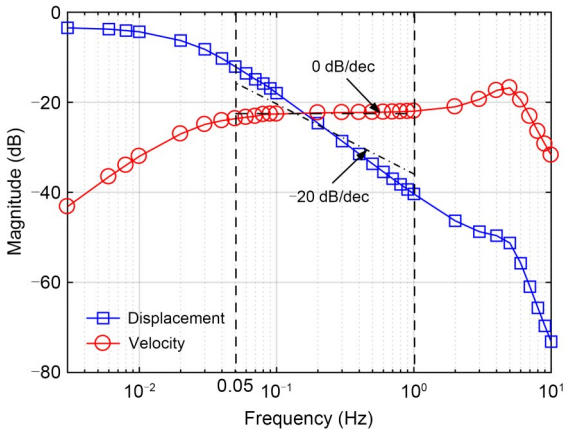

Fig. 7 Magnitude–frequency characteristic curves of displacement and velocity

4.3 Analysis of experimental results

The distortion of the vibration waveform was concentrated mainly in the first five harmonics. The harmonic amplitude was obtained from the Fourier transform, and the THD γ of the vibration waveform was calculated by Eq. (13), where A_1 is the fundamental frequency amplitude and A_i (i=2, 3, 4, 5) is the i^{th} harmonic amplitude (Li C et al., 2022). To highlight the harmonic suppression effect of different control methods, the relative difference γ_e of THD between different methods and open-loop control was calculated by Eq. (14), where γ_o denotes the THD of the open-loop system.

$$\gamma = \frac{1}{A_1}\sqrt{\sum_{i=2}^{5} A_i^2} \times 100\%, \tag{13}$$

$$\gamma_e = \frac{\gamma - \gamma_o}{\gamma_o} \times 100\%. \tag{14}$$

The power resistor R_s was connected in series on one side of the driving circuit. The u_v was calculated by Eq. (8) and amplified by K_v times in the controller to output the feedback signal via DAC. The driving voltage u_a was obtained from the output voltage observation port of the power amplifier; the driving current i was obtained by measuring the voltage across R_s, and when R_s=0, i was measured by the output current observation port of the power amplifier (depending on the actual conditions, a non-contact current sensor can also measure i without a sampling resistor). With K_v set at 0.3, the power resistor R_s with different resistance values was used to analyze its effect on γ, and the open-loop system was adopted for comparison. The experimental results are shown in Fig. 8: (1) With increasing vibration frequency, the same vibration amplitude required greater driving force, the signal-to-noise ratio was high, the insensitivity to interference was strengthened, and the THD gradually decreased. (2) When the experimental frequency point approached both ends of the velocity characteristic frequency band, the ability of velocity feedback to improve the waveform was weakened. (3) In the velocity characteristic frequency band, the use of the sampling resistor changed the original driving circuit structure. As R_s increased, the capability of the sensorless velocity feedback control to improve the THD of the vibration waveform decreased. Therefore, R_s=0 was selected; that is, the driving current was recommended to be obtained through the output current observation port of the power amplifier.

When R_s=0, K_v was set to different values to analyze its effect on γ. The experimental results are shown in Fig. 9. The trend of THD of the vibration waveform for different values of K_v was similar to that for different values of R_s (Fig. 8), but with increasing K_v, the suppression ability of velocity feedback was enhanced. The improvement of γ and γ_e was no longer significant once K_v increased from 0.3 to 0.4, and thus K_v=0.3 was selected.

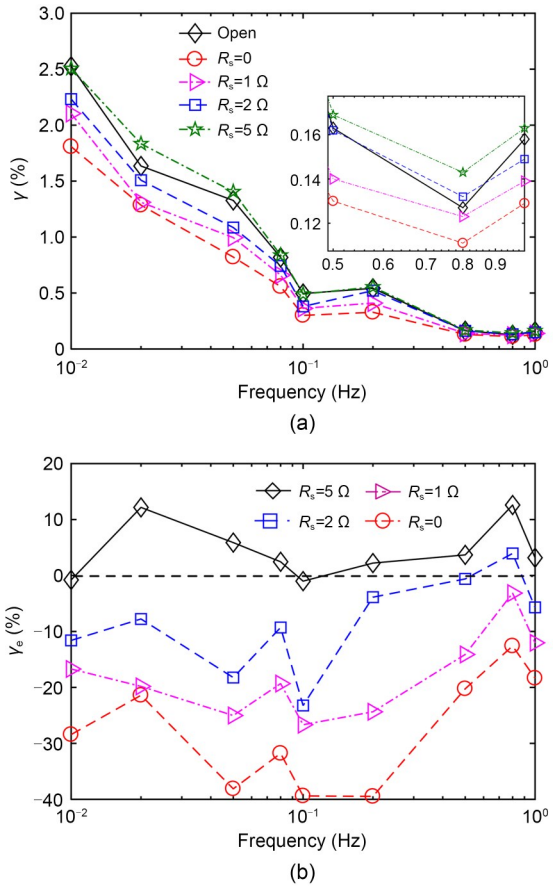

Fig. 8 Influence of different R_s's on velocity feedback control: (a) γ; (b) γ_e

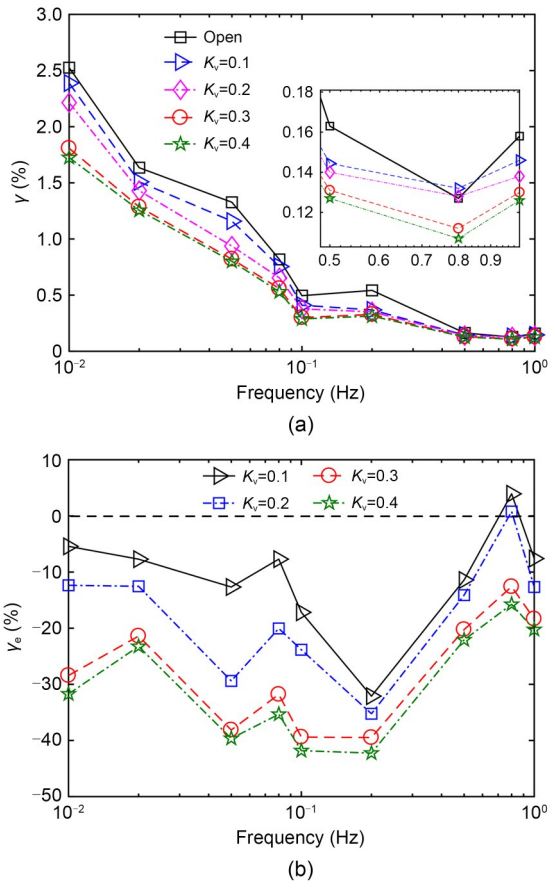

Fig. 9 Influence of different K_v's on velocity feedback control: (a) γ; (b) γ_e

Finally, based on the results of the above experiments, R_s=0 and K_v=0.3 were selected as the parameter values for velocity feedback control in this study, and R'=R_{ac} was set to ensure high accuracy of velocity extraction. The R_{ac} was calculated before the experiment. At the experimental frequency, the vibration velocity $\dot{x}$, driving voltage u_a, and current i were measured, and the corresponding R_{ac} was calculated accurately by Eq. (8), where $\dot{x}$ was obtained by differential calculation of the vibration displacement. According to the analysis in Section 3, the phase difference between the feedback signal and the reference input determines the ability of feedback control to suppress THD. Therefore, the effectiveness of the proposed method should be evaluated by the phase accuracy of the extracted velocity. The phase of the measured displacement signal was φ_x, the phase of the extracted velocity signal was φ_{Ex}, and their phase difference was $\Delta\varphi$=φ_{Ex}−φ_x. As shown in Fig. 10, $\Delta\varphi$ was less than 90° due to neglecting the inductance L. The value of L became smaller as the frequency increased (Chen and Liaw, 1999; Della Flora and Gründling, 2008). $\Delta\varphi$ approached 90°, while the curve of R'=R_{ac} was closer to 90°. The proposed method improved the velocity extraction accuracy of the conventional method.

To fully illustrate the superiority of our proposed method, it was compared with open-loop control, the conventional displacement feedback control method based on expensive displacement sensors (displacement feedback coefficient K_x=1), and the conventional sensorless feedback control method based on sampling resistance and obtaining vibration information through the DC equivalent resistance of the coil (setting R_s=1 Ω, R'=R_{dc}+R_s, and velocity feedback coefficient K_{vdc}=0.3), where R_{dc} was measured in advance by a multimeter. To emphasize the innovation of the method proposed in this study, we also compared it with the sensorless velocity feedback control method based on Kalman filter estimation proposed by Li W et al. (2023). Table S1 in the supplementary materials presents the first five harmonic amplitudes and γ of the vibration waveforms obtained by the different methods. Fig. 11 shows the time-domain vibration waveforms at 0.05 and 0.50 Hz. As the vibration frequency decreased, the electromagnetic driving force and the anti-interference capability decreased, and the γ of the vibration waveform became larger and was disturbed mainly by the first two harmonics. Fig. 12 compares the THD suppression capabilities of the different feedback methods to show the changing trends.

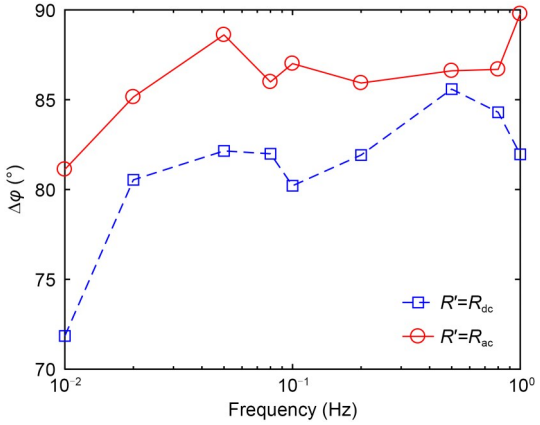

Fig. 10 $\Delta\varphi$ of different vibration velocity extraction methods

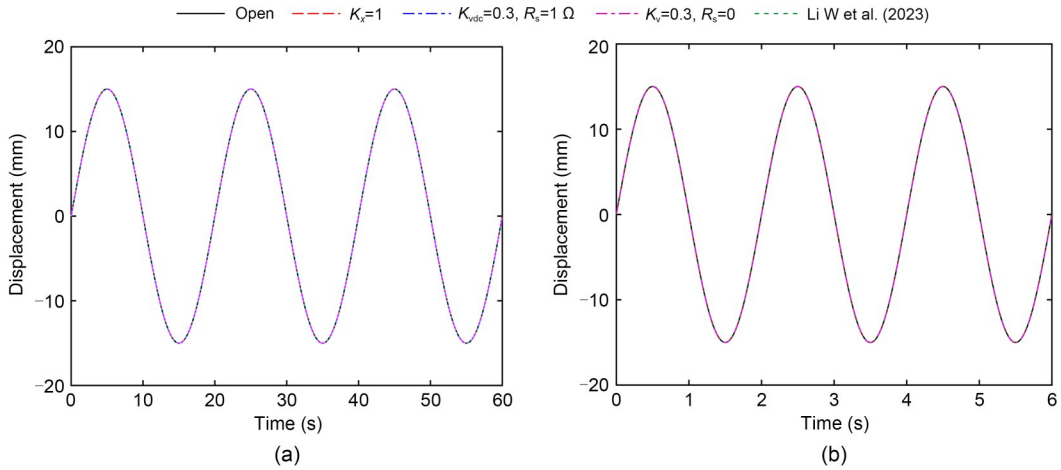

Fig. 11 Time-domain vibration waveforms of different control methods: (a) 0.05 Hz; (b) 0.50 Hz

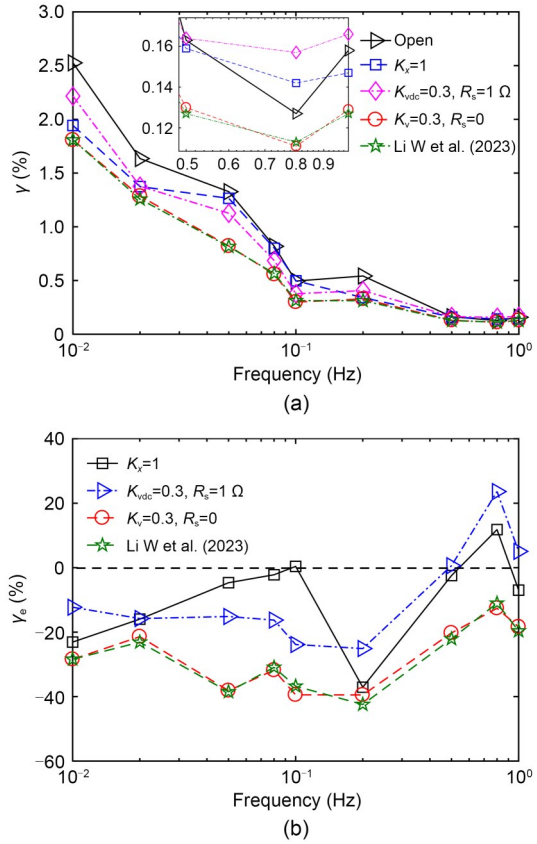

Fig. 12 Comparison of the THD suppression abilities of different control methods: (a) γ; (b) γ_e

Fig. 12 shows the following: (1) In the velocity characteristic frequency band, high-precision sensorless feedback control has a strong THD suppression ability, reducing the vibration waveform THD by about 40% relative to open-loop control. (2) The displacement feedback control method has a limited ability to suppress THD in the experimental frequency band. Nevertheless, the waveform improvement effect is gradually strengthened at the lower frequency points close to the displacement characteristic frequency band. (3) Conventional sensorless feedback control methods have limited ability to extend the velocity characteristic frequency band due to the need for sampling resistors, and can reduce vibration waveform THD only in a smaller frequency range (from 0.02 to 0.20 Hz) compared with conventional displacement feedback control. (4) The conventional sensorless feedback control method estimates the vibration velocity with lower accuracy compared with the open-loop control method. The THD of the vibration waveform can be reduced by only about 20%. Therefore, our proposed method has a better THD suppression effect. (5) The method proposed by Li W et al. (2023) has a THD suppression capability comparable to or even slightly stronger than that of our proposed method. However, it has the following drawbacks: First, the estimation of velocity based on the Kalman filter requires a high computational power of the controller. Second, the velocity estimation accuracy of the Kalman filter depends on accurate selection of process noise covariance and measurement noise covariance, and the selection process can often be accomplished only by a trial-and-error method, which is a complex process. Third, the Kalman filter estimates the velocity with measured displacement as a known quantity and therefore is not a valid sensorless control method.

5 Conclusions

The sensorless velocity feedback control method is crucial in reducing the THD of low-frequency vibration waveforms and improving vibration calibration accuracy. This study presents an improved sensorless velocity feedback control method for electromagnetic vibrators to improve the sensorless velocity extraction accuracy and interference suppression capability of the conventional method. The main conclusions are as follows:

1. The use of AC resistors improves the accuracy of vibration velocity estimation. The harmonic interference introduced by the velocity estimation error, which is difficult to suppress with feedback control, is reduced.

2. The ability of sensorless velocity feedback control to suppress interference declines as sampling resistance increases. Therefore, sampling resistors should not be used to obtain the driving current.

3. The proposed method reduces the THD of the vibration waveform by about 20% compared to the conventional sensorless velocity feedback control method.

4. The proposed method has a THD suppression capability comparable to that of a recent advanced method. However, the proposed method has a simpler parameter adjustment process that does not use sensors and is more reliable, less costly, and easier to maintain.

The main contribution of this study is the proposed improved method of sensorless velocity feedback

control, which can be implemented with analog circuits. According to the experimental results, the proposed method is simple and reliable, and has a low cost and high value in engineering applications for improving low-frequency vibration calibration accuracy. Subsequent work will focus on applying the sensorless velocity extraction method combined with other advanced control algorithms to further improve the performance of electromagnetic vibrators.

Contributors

Wei LI and Junning CUI designed the research. Wei LI and Xingyuan BIAN processed the data. Wei LI drafted the paper. Junning CUI and Limin ZOU helped organize the paper. Junning CUI revised and finalized the paper.

Conflict of interest

All the authors declare that they have no conflict of interest.

Data availability

The data that support the findings of this study are available from the corresponding author upon reasonable request.

References

Addari D, Aglietti GS, Remedia M, 2017. Experimental and numerical investigation of coupled microvibration dynamics for satellite reaction wheels. *J Sound Vib*, 386:225-241. https://doi.org/10.1016/j.jsv.2016.10.003

Chen TH, Liaw CM, 1999. Vibration acceleration control of an inverter-fed electrodynamic shaker. *IEEE/ASME Trans Mech*, 4(1):60-70. https://doi.org/10.1109/3516.752085

Chi QL, Shang SK, 2018. On the extraction technique of the single-coil self-feedback signal on a standard vibration table. *J Vib Contr*, 24(18):4316-4324. https://doi.org/10.1177/1077546317723763

Crawford WC, Webb SC, 2000. Identifying and removing tilt noise from low-frequency (<0.1 Hz) seafloor vertical seismic data. *Bull Seismol Soc Am*, 90(4):952-963. https://doi.org/10.1785/0119990121

Cui JN, He ZQ, Tan JB, 2017. Proposal and analysis of three closed double magnetic circuits to obtain a very long stroke for electrodynamic force generators. *Sens Actuat A Phys*, 263:122-130. https://doi.org/10.1016/j.sna.2017.05.049

Cui JN, Li W, Bian XY, et al., 2020. Rectangular closed double magnetic circuit offering ultra-long stroke for ultra-low-frequency vibration exciter. *Appl Sci*, 10(17):6118. https://doi.org/10.3390/app10176118

Della Flora L, Gründling HA, 2008. Time domain sinusoidal acceleration controller for an electrodynamic shaker. *IET Contr Theory Appl*, 2(12):1044-1053. https://doi.org/10.1049/iet-cta:20080188

Garg N, Schiefer MI, 2017. Low frequency accelerometer calibration using an optical encoder sensor. *Measurement*, 111:226-233. https://doi.org/10.1016/j.measurement.2017.07.031

Garrido R, Luna L, 2021. Robust ultra-precision motion control of linear ultrasonic motors: a combined ADRC-Luenberger observer approach. *Contr Eng Pract*, 111:104812. https://doi.org/10.1016/j.conengprac.2021.104812

He W, Zhang XF, Wang CY, et al., 2014. A long-stroke horizontal electromagnetic vibrator for ultralow-frequency vibration calibration. *Meas Sci Technol*, 25(8):085901. https://doi.org/10.1088/0957-0233/25/8/085901

ISO, 1999. Methods for the Calibration of Vibration and Shock Transducers—Part 11: Primary Vibration Calibration by Laser Interferometry. ISO 16063-11:1999. International Organization for Standardization, Geneva, Switzerland.

Lang GF, 1997. Electrodynamic shaker fundamentals. *SV Sound Vib*, 31(4):14-23.

Lang GF, Snyder D, 2001. Understanding the physics of electrodynamic shaker performance. *SV Sound Vib*, 35(10): 24-33.

Li C, Chen ZW, 2020. A fast vibration-level adjustment method for low-frequency vibration calibration based on modified filtered-x least mean square algorithm. *Meas Contr*, 53(3-4):328-338. https://doi.org/10.1177/0020294019881727

Li C, Mao CT, Chen ZW, 2022. A novel adaptive control algorithm for the rejection of harmonics in a standard vibrator. *J Vib Contr*, 28(3-4):439-451. https://doi.org/10.1177/1077546320980200

Li L, Xu WX, Tan YF, et al., 2023a. Fluid-induced vibration evolution mechanism of multiphase free sink vortex and the multi-source vibration sensing method. *Mech Syst Signal Process*, 189:110058. https://doi.org/10.1016/j.ymssp.2022.110058

Li L, Tan YF, Xu WX, et al., 2023b. Fluid-induced transport dynamics and vibration patterns of multiphase vortex in the critical transition states. *Int J Mech Sci*, 252:108376. https://doi.org/10.1016/j.ijmecsci.2023.108376

Li W, Cui JN, Bian XY, et al., 2023. Velocity feedback control method of low-frequency electromagnetic vibration exciter based on Kalman filter estimation. *Rev Sci Instrum*, 94(3): 035006. https://doi.org/10.1063/5.0134290

Liu ZH, Cai CG, Lv Q, et al., 2021. Improved control of linear motors for broadband transducer calibration. *IEEE Trans Instrum Meas*, 70:1004910. https://doi.org/10.1109/TIM.2021.3057329

Ohno K, Ito K, Yamada T, et al., 2021. Disturbance suppression considering thrust constant fluctuation and restoring force of flat cable for precise force control. *IEEE Trans Ind Electron*, 68(1):882-891. https://doi.org/10.1109/TIE.2020.3016248

Okwudire CE, Lee J, 2013. Minimization of the residual vibrations of ultra-precision manufacturing machines via optimal placement of vibration isolators. *Prec Eng*, 37(2):425-432. https://doi.org/10.1016/j.precisioneng.2012.11.005

Okyay A, Khamesee MB, Erkorkmaz K, 2015. Design and optimization of a voice coil actuator for precision motion applications. *IEEE Trans Magn*, 51(6):8202811. https://doi.org/10.1109/TMAG.2014.2381160

Rana KPS, 2011. Fuzzy control of an electrodynamic shaker for automotive and aerospace vibration testing. *Expert Syst Appl*, 38(9):11335-11346. https://doi.org/10.1016/j.eswa.2011.02.184

Repecho V, Waqar JB, Biel D, et al., 2022. Zero speed sensorless scheme for permanent magnet synchronous machine under decoupled sliding-mode control. *IEEE Trans Ind Electron*, 69(2):1288-1297. https://doi.org/10.1109/TIE.2021.3062260

Ripper GP, Dias RS, Garcia GA, 2009. Primary accelerometer calibration problems due to vibration exciters. *Measurement*, 42(9):1363-1369. https://doi.org/10.1016/j.measurement.2009.05.002

Scott DA, Dickinson LP, 2014. Distortion effects in primary calibration of low-frequency accelerometers. *Metrologia*, 51(3):212-224. https://doi.org/10.1088/0026-1394/51/3/212

Shimoda T, Kokuyama W, Nozato H, 2021. Primary calibration system for digital accelerometers. *Metrologia*, 58(4): 045002. https://doi.org/10.1088/1681-7575/ac0403

Shuang B, Zhu ZQ, Wu XM, 2022. Improved cross-coupling effect compensation method for sensorless control of IPMSM with high frequency voltage injection. *IEEE Trans Energy Conv*, 37(1):347-358. https://doi.org/10.1109/TEC.2021.3093361

Uchiyama Y, Mukai M, Fujita M, 2009. Robust control of electrodynamic shaker with 2DoF control using H_∞ filter. *J Sound Vib*, 326(1-2):75-87. https://doi.org/10.1016/j.jsv.2009.04.024

Wang GL, Valla M, Solsona J, 2020. Position sensorless permanent magnet synchronous machine drives—a review. *IEEE Trans Ind Electron*, 67(7):5830-5842. https://doi.org/10.1109/TIE.2019.2955409

Xiao DX, Ye J, Fang GL, et al., 2022. A regional phase-locked loop-based low-speed position-sensorless control scheme for general-purpose switched reluctance motor drives. *IEEE Trans Power Electron*, 37(5):5859-5873. https://doi.org/10.1109/TPEL.2021.3130273

Xiao LF, Ma LM, Huang XH, 2022. Intelligent fractional-order integral sliding mode control for PMSM based on an improved cascade observer. *Front Inform Technol Electron Eng*, 23(2):328-338. https://doi.org/10.1631/FITEE.2000317

Yildiz R, Barut M, Zerdali E, 2020. A comprehensive comparison of extended and unscented Kalman filters for speed-sensorless control applications of induction motors. *IEEE Trans Ind Inform*, 16(10):6423-6432. https://doi.org/10.1109/TII.2020.2964876

Zhang XF, He W, Wang CY, 2017. Self-sensing waveform control for a low-frequency electromagnetic vibrator. *IEEE/ASME Trans Mech*, 22(2):785-793. https://doi.org/10.1109/TMECH.2016.2635260

List of supplementary materials

Fig. S1 Schematic diagram of low-frenquency dual magnetic circuit horizontal vibrators

Fig. S2 Bode diagram for different values of K_v when R_s is a constant value

Fig. S3 Bode diagram for different values of R_s when K_v is a constant value

Fig. S4 Root locus of closed-loop system about K_v

Table S1 Amplitudes of the harmonics and total harmonic distortion